Journal of Thermal Analysis and Calorimetry (2022) 147:10637–10646
https://doi.org/10.1007/s10973-022-11268-w

Numerical investigation of fluid flow and heat transfer in micropolar fluids over a stretching domain

Maheshwar Pathak[1] · **Pratibha Joshi**[1] · **Kottakkaran Sooppy Nisar**[2]

Received: 26 July 2021 / Accepted: 5 February 2022 / Published online: 10 March 2022

Abstract

In the present paper, fluid flow and heat transfer for micropolar fluids over a stretching sheet through Darcy porous medium are studied. The heat transfer phenomenon is considered with the isothermal wall as well as the isoflux boundary conditions. The fluid flow and heat transfer phenomena are modeled in the form of coupled nonlinear partial differential equations. The numerical solution is obtained using a nonstandard finite difference approximation on a quasi-uniform mesh. The numerical results obtained by the present approach are compared to those obtained by the Runge–Kutta fourth order method to demonstrate the accuracy of the present method. The numerical results obtained by both methods show excellent agreement. The effect of various physical parameters, namely the Reynolds number, Prandtl number, micropolar material parameters, injection/suction parameter, heat index parameter on bulk fluid speed, temperature distribution, and spin behavior of microstructures are demonstrated and discussed graphically. The simplicity of the finite difference approximation makes the selected technique more significant in the numerical study of micropolar fluid. The boundary layer thickness reduces with the increasing value of injection/suction parameter, Reynolds number, and micropolar parameter. The thermal boundary layer also reduces with the increment in the value of the micropolar parameter, Prandtl number, heat index parameter while microrotation increases with the increasing value of the injection/suction parameter.

Keywords Micropolar fluids · Heat transfer · Boundary layer thickness · Microrotation · Quasi-uniform mesh

Mathematics Subject Classification 76S05 · 76A05 · 80M20 · 65L12

Nomenclature

∇	Gradient operator
ρ	Density of the fluid
$\mathbf{U}$	Velocity of the fluid
t	Time coordinate
$\mathbf{W}$	Microrotation vector
$\mathbf{f_b}$	Body force
$\mathbf{l}$	Body couple per unit mass
P	Fluid pressure
j	Micro inertia
λ_c	Stokes viscosity
μ_c	Dynamic viscosity
κ_c	Vortex viscosity
γ_c	Spin viscosity
α_c, β_c	Additional viscosity coefficients
U_0	Wall velocity coefficients
L	Length of porous sheet
x	Flow direction along the stretching sheet
y	Perpendicular direction to the stretching sheet
u	Velocity in x direction
v	Velocity in y direction
ω_3	Component of microrotation perpendicular to xy−plane
T	Fluid temperature
α_{eff}	Effective thermal diffusivity
v_w	Injection velocity
q_0	Wall heat flux coefficient

✉ Maheshwar Pathak
mpathak81@gmail.com

Pratibha Joshi
pratibha.joshi@gmail.com

Kottakkaran Sooppy Nisar
n.sooppy@psau.edu.sa

[1] Department of Mathematics, University of Petroleum and Energy Studies, Bidholi (P.O.), Via Prem Nagar, Dehradun 248007, India

[2] Department of Mathematics College of Arts and Sciences, Prince Sattam Bin Abdulaziz University, Al-Kharj, Saudi Arabia

τ	Effective thermal conductivity
s	Heat index parameter
K	Permeability of the porous medium
η	Dimensionless similarity variable
ψ	Stream function
f	Similarity function for velocity
H	Dimensionless Microrotation
c_1, c_2, c_3	Dimensionless material constants
θ	Dimensionless temperature
R_e	Reynolds number
P_r	Prandtl number
λ	Mass injection/suction parameter
N	Number of subintervals in quasi-uniform mesh

Introduction

Extensive usage of different types of fluids in various industrial and engineering applications makes the study of heat and mass transfer for these fluids more desirable [1–7]. Micropolar fluids are subclass of microfluids [8]. In these fluids, randomly oriented rigid spherical particles having their own spins and microrotation where the deformation of fluid particles is not allowed are suspended in a viscous medium [9]. Some classic examples of micropolar fluids are human and animal blood, salty water, dusty fluids, polymeric fluids, liquid crystals, lubricants, colloidal suspension, and dilute solutions with long-chain atomic structures. Fluid flow due to stretching sheet can be seen in a variety of industry and engineering applications, such as a chemical engineering plant's polymer processing unit, aerodynamic extrusion of plastic sheets, annealing of copper wires, hot rolling, fiber glass, drawing of plastic films, and paper production. Wide applications of this type of flow make researchers more interested in their study. Sakiadis [10–12] presented the theoretical analysis of boundary layer flow over a continuous solid surface moving at constant speed in 1961. Crane [13] expanded further Sakiadis' work in 1970, exploring at fluid flow caused by stretching sheets. Bachok et al. [14] investigated the unsteady laminar flow of an incompressible micropolar fluid across a stretching sheet in 2011. The stagnation point flow of an incompressible micropolar fluid over a stretching sheet was studied by Nazar et al. [15] in 2004. Mohanty et al. [16] published a numerical study on the heat and mass transfer effect of a micropolar fluid across a stretching sheet through porous medium in 2015. In 2019, Mandal and Mukhopadhyay analyzed [17] behavior of boundary layer flow under the influence of nonlinear convection. Jain and Gupta [18] performed entropy generation analysis of micropolar fluid flow with radiation and thermal slip in 2019. In 2020, Ramadevi et al. [19] numerically studied 2D magnetohydrodynamic nonlinear radiative flow of micropolar fluid. Some more study for the micropolar fluids can be found easily in the literature [20–26].

Darcy law, which is applicable for flow with a small velocity or Reynolds number, is used to formulate viscous flow into porous media. Porous medium is a solid body that contains small void spaces (pores), which are distributed more or less throughout the body. In the study of viscous flow of micropolar fluids through porous media, many analytical and numerical techniques have been used previously. In [27], variation of parameters technique was used to find analytical solutions of laminar viscous flow in non-Darcy porous medium of micropolar fluid encountering uniform suction/injection. In [28], homotopy analysis method has been applied for the study of micropolar fluid flow. Quasilinearization technique is applied to study fluid flow of micropolar fluid in [29–31]. In [32], finite difference method along with successive over relaxation method has been used for numerical investigation of micropolar fluid flow with porous medium. Fourier sine transform technique [33], Adomian decomposition method [34], homotopy perturbation method [35], Nachtsheim–Swigert iteration method [36], coupling of Runge–Kutta technique and shooting method [37–39], etc., are some techniques which were used in the study of fluid flow of micropolar fluids through porous media.

Most of the methods used in the study of micropolar fluid previously are cumbersome due to their semi-analytical nature. In addition, many methods depend on a very accurate initial solution. Due to these difficulties in the previously used methods, one needs to use a more simple and effective method for the study of fluid flow and thermal behavior of the micropolar fluids. Considering the simplicity and effectiveness of the finite difference approximation and classical Newton's method, we have selected this combination for the current study. The key objective of this study is to investigate the effect of various flow parameters on the fluid flow, microrotation of microstructures present in the fluid, and thermal behavior of micropolar fluids. A detailed description of the present method is given in the method of solution section. In addition, a detailed investigation of the main objective of the current work is presented in the result and discussion section.

The numerical results obtained by the nonstandard finite difference approximation on a quasi-uniform mesh were compared with those obtained by the Runge–Kutta method. The numerical results obtained by both methods are in excellent agreement that validates our findings. The effect of various flow parameters on velocity, microrotation, and temperature distribution is demonstrated graphically in the result and discussion section. Finally, the work is concluded in the conclusion section.

Mathematical model

The theory of micropolar fluids are formulated by considering the principle of conservation of local angular momentum along with principle of conservation of mass and momentum [9]. The governing field equations of the motion are given as [8, 9]: Conservation of mass:

$$\frac{\partial \rho}{\partial t} + \nabla\cdot(\rho \mathbf{U}) = 0, \tag{1}$$

Conservation of momentum:

$$\begin{aligned}&(\lambda_c + 2\mu_c + \kappa_c)\nabla(\nabla\cdot\mathbf{U}) + \kappa_c \nabla\times\mathbf{W} - \nabla P\\&\quad - (\mu_c+\kappa_c)\nabla\times\nabla\times\mathbf{U} + \rho\mathbf{f}_b\\&= \rho\frac{D\mathbf{U}}{Dt},\end{aligned} \tag{2}$$

local angular momentum conservation:

$$\begin{aligned}&(\alpha_c + \beta_c + \gamma_c)\nabla(\nabla\cdot\mathbf{W}) - \gamma_c\nabla\times\nabla\times\mathbf{W}\\&\quad + \kappa_c\nabla\times\mathbf{U} - 2\kappa_c\mathbf{W} + \rho\mathbf{1}\\&= \rho j\frac{D\mathbf{W}}{Dt},\end{aligned} \tag{3}$$

here, $\mathbf{U}, \mathbf{W}, \rho, \mathbf{f}_b, \mathbf{1}, P, j$ are velocity vector, microrotation vector, density, body force, body couple per unit mass, pressure, micro-inertia, respectively, and $\lambda_c, \mu_c, \kappa_c, \gamma_c$ are Stokes viscosity, dynamic viscosity, vortex viscosity, spin gradient viscosity, respectively. α_c and β_c are material constants.

Consider the steady, 2–D incompressible flow of a micropolar fluid. Flow is considered across a homogeneous porous medium over a porous stretching sheet, assuming that the body force and the body couple are negligible. The permeability of porous medium is K. Fluid flow is affected due to linear stretching of a permeable sheet of length L along the x–axis. Flow linear velocity is $U_w = U_0 x/L$ in the direction of x–axis (along with the sheet). Under these assumptions Eqs. (1)–(3) gives:

$$\frac{\partial u}{\partial x} + \frac{\partial v}{\partial y} = 0, \tag{4}$$

$$\begin{aligned}&(\mu_c+\kappa_c)\left(\frac{\partial^2 u}{\partial x^2} + \frac{\partial^2 u}{\partial y^2}\right) + \kappa_c\frac{\partial \omega_3}{\partial y} - \frac{\mu_c}{K}u\\&\quad = \rho\left(u\frac{\partial u}{\partial x} + v\frac{\partial u}{\partial y}\right),\end{aligned} \tag{5}$$

$$\gamma_c\frac{\partial^2\omega_3}{\partial y^2} - 2\kappa_c\omega_3 + \kappa_c\frac{\partial u}{\partial x} = \rho j v\frac{\partial \omega_3}{\partial y}, \tag{6}$$

where u and v are horizontal and vertical velocity components in the directions of x–axis and y–axis. ω_3 is the microrotation's component perpendicular to xy–plane.

The energy equation is:

$$u\frac{\partial T}{\partial x} + v\frac{\partial T}{\partial y} = \alpha_{\mathrm{eff}}\frac{\partial^2 T}{\partial y^2}, \tag{7}$$

where T is the fluid temperature and α_{eff} is the effective thermal diffusivity.

The hydrodynamic boundary conditions are:

$$\begin{aligned}&u(x^*,0) = U_0 x^*,\ v(x^*,0) = v_w,\ \omega_3(x^*,0) = -m\frac{\partial u}{\partial y},\\&\qquad u(x^*,\infty) = 0,\ -\omega_3(x^*,\infty) = 0,\end{aligned} \tag{8}$$

where $x^* = x/L$ is the nondimensional x–coordinate with permeable sheet's length L, U_0 is wall velocity coefficient which is constant, v_w is injection velocity and m is constant such that $0 \le m \le 1$. $m = 0$ case is called a strong concentration [40]. The concentrated particle flows in this situation, preventing the microelements adjacent to the wall surface from rotating [41]. The case $m = 0.5$ denotes weak concentrations and in this case the stress tensor's antisymmetric part vanishes [42].The turbulent boundary layer flows are modeled using the $m = 1$ case [43]. The thermal boundary conditions considered are:

$$\begin{aligned}&T(x^*,0) = T_\infty + T_0(x^*)^s,\ T(x^*,\infty) = T_\infty \ \text{Power-law temperature},\\&-\tau\left.\frac{\partial T}{\partial y}\right|_{(x^*,0)} = q_0(x^*)^s,\ T(x^*,\infty) = T_\infty \ \text{Power-law heat flux,}\end{aligned} \tag{9}$$

where T_0 is wall temperature coefficient, T_∞ temperature far away from the sheet, q_0 is wall heat flux coefficient, τ is the medium's effective thermal conductivity and s is power law index.

The following similarity transformation is used to generate the dimensionless form of the aforementioned equations:

$$\begin{aligned}&\eta = \frac{y}{\sqrt{K}},\ \psi = U_0 x^*\sqrt{K}f(\eta),\\&u = U_0 x^* f'(\eta),\ v = -\frac{U_0}{L}\sqrt{K}f(\eta),\ \omega_3 = \frac{U_0 x^*}{\sqrt{K}}H(\eta)\end{aligned} \tag{10}$$

where ψ is stream function, $\partial\psi/\partial y = u$, $-\partial\psi/\partial x = v$ and $f' = \mathrm{d}f/\mathrm{d}\eta$. Under the similarity transformation (10), (5)–(7) are transformed into following coupled nonlinear ordinary differential equations:

$$(1 + c_1)f''' + R_e(ff'' - f'^2) - f' + c_1 H' = 0, \tag{11}$$

$$H'' - c_1c_2(f'' - 2H) - c_3(f'H - fH') = 0, \tag{12}$$

$$\theta'' + P_r R_e(f\theta' - sf'\theta) = 0, \tag{13}$$

where prime denotes the differentiation with respect to η, P_r is the Prandtl number, $R_e = \rho U_0 K/L\mu_c$ is the Reynolds number, $c_1 = \kappa_c/\mu_c, c_2 = \kappa_c\mu_c/\gamma_c, c_3 = \rho j\kappa_c\mu_c/\gamma_c$ are dimensionless material constants.

Equations (8) and (9) give:

$$\begin{aligned} &f(0)=\lambda,\ f'(0)=1,\ f'(\infty)=0,\\ &H(0)=0,\ H(\infty)=0,\\ &\theta(0)=1,\ \theta(\infty)=0, \qquad \text{(Isothermal)},\\ &\theta'(0)=-1,\ \theta'(\infty)=0, \qquad \text{(Isoflux)}, \end{aligned} \tag{14}$$

where $\lambda = -v_w L/U_0\sqrt{K}$ is the mass suction/injection parameter. Positive λ is called mass suction parameter and negative λ is called mass injection parameter.

The physical quantities of interest are the local wall shear stress τ_w, the wall couple stress m_w and the heat transfer from sheet surface q_w which are defined as [44]:

$$\tau_w = \left[(\mu_c+\kappa_c)\frac{\partial u}{\partial y} + \kappa_c H\right]_{y=0},$$
$$m_w = \gamma_c\left[\frac{\partial H}{\partial y}\right]_{y=0},\quad q_w = -\left[\tau\frac{\partial T}{\partial y}\right]_{y=0}.$$

Method of solution

The nonstandard finite difference approximation has been used to solve the boundary value problem (11)–(14). Quasi-uniform mesh is used to discretized BVP (11)–(14). The isothermal and isoflux boundary conditions considered separately in the solution procedure. To apply proposed method, we transformed the BVP (11)–(14) into a system of ordinary differential equations of first order as follows:

$$\begin{aligned} \frac{dg_1}{d\eta} &= g_2,\\ \frac{dg_2}{d\eta} &= g_3,\\ \frac{dg_3}{d\eta} &= \frac{1}{(1+c_1)}\left[-R_e\left(g_1g_3-g_2^2\right)+g_2-c_1g_5\right],\\ \frac{dg_4}{d\eta} &= g_5,\\ \frac{dg_5}{d\eta} &= c_1c_2\left(g_3-2g_4\right)+c_3\left(g_2g_4-g_1g_5\right),\\ \frac{dg_6}{d\eta} &= g_7,\\ \frac{dg_7}{d\eta} &= -P_rR_e\left(g_1g_7-sg_2g_6\right), \end{aligned} \tag{15}$$

with boundary conditions

$$\begin{aligned} &g_1(0)=\lambda,\ g_2(0)=1,\ g_2(\infty)=0,\\ &g_4(0)=0,\ g_4(\infty)=0,\\ &g_6(0)=1,\ g_6(\infty)=0, \qquad \text{(Isothermal)},\\ &g_7(0)=-1,\ g_7(\infty)=0, \qquad \text{(Isoflux)}, \end{aligned} \tag{16}$$

where $g_1 = f, g_2 = f', g_3 = f'', g_4 = H, g_5 = H', g_6 = \theta$ and $g_7 = \theta'$.

In the present method, strictly monotone smooth quasi-uniform map $\eta = \eta(\xi)$ has been considered. This quasi-uniform map is called grid generating function and defined as [45]:

$$\eta = -cp\cdot\ln(1-\xi), \tag{17}$$

where $\xi \in [0,1], \eta \in [0,\infty]$ and cp is a control parameter. The uniform grids $\xi_n = n/N; n = 0,1,2,\dots,N$ defined on interval [0, 1] with $\xi_0 = 0$ and $\xi_{n+1} = \xi_n + h$ with $h = 1/N$ generated a quasi-uniform grids $\eta_n = \eta(\xi_n)$ on the interval $[0,\infty]$. The last interval $[\eta_{N-1},\eta_N]$ is infinite. The midpoint $\eta_{N-1/2}$ of interval $[\eta_{N-1},\eta_N]$ is finite, because at the non-integer nodes the quasi uniform grids are defined as

$$\eta_{n+\delta} = \eta\left(\xi = \frac{n+\delta}{N}\right),$$

with $n \in \{0,1,2,\dots,N-1\}$ and $\delta \in (0,1)$. The infinite domain is represented by the finite number of intervals using the quasi-uniform map. The last node η_N of this mesh is placed at infinity so that the right-side boundary condition is taken into account properly.

The scalar function $g(\eta)$ and its first derivative $g'(\eta)$ at midpoints $\eta_{n+\frac{1}{2}}, n = 0,1,2,\dots,N-1$, applying nonstandard finite difference approximation are approximated as [46]:

$$g_{n+\frac{1}{2}} \approx \frac{\eta_{n+\frac{3}{4}}-\eta_{n+\frac{1}{2}}}{\eta_{n+\frac{3}{4}}-\eta_{n+\frac{1}{4}}}g_n + \frac{\eta_{n+\frac{1}{2}}-\eta_{n+\frac{1}{4}}}{\eta_{n+\frac{3}{4}}-\eta_{n+\frac{1}{4}}}g_{n+1}, \tag{18}$$

$$\left.\frac{dg}{d\eta}\right|_{n+\frac{1}{2}} \approx \frac{g_{n+1}-g_n}{2\left(\eta_{n+\frac{3}{4}}-\eta_{n+\frac{1}{4}}\right)}, \tag{19}$$

where $g_n = g(\eta_n)$. Formulae (18)–(19) use the value $g_N = g_\infty$ without using last grid point $\eta_N = \infty$. The order of accuracy of the approximation formulae (18) and (19) are $O\left(N^{-2}\right)$.

Using nonstandard finite difference approximations (18) and (19) into system (15)–(16), we get a nonlinear system of equations with $7\cdot(N+1)$ equations and $7\cdot(N+1)$ unknowns namely $g_i^{[n]}$ for $i = 1,2,\dots,7$ and $n = 0,1,2,\dots,N$, where $g_i^{[n]} = g_i(\eta_n)$.

Newton's method is used for the solution of obtained nonlinear system of $7\cdot(N+1)$ equations. In the solution by Newton's method, the following simple termination criterion has been used

$$\left|\Delta g_i^{[n]}\right| \le \text{TOL} \quad \text{for } i = 1,2,\dots,7 \text{ and } n = 0,1,2,\dots,N,$$

where $\Delta g_i^{[n]}$ is the difference of two successive iterations of $g_i^{[n]}$ and TOL represents a fixed tolerance. In the next section, all the numerical computations were performed by fixing

Table 1 Results by Runge–Kutta method (RKM) and present method with $N = 201$ (Isothermal)

η	$f(\eta)$		$f'(\eta)$	
	RKM	Present method	RKM	Present method
0.0	0.00000	0.00000	1.00000	1.00000
0.5	0.38034	0.38037	0.56288	0.56287
1.0	0.59431	0.59435	0.31640	0.31639
1.5	0.71444	0.71450	0.17733	0.17732
2.0	0.78163	0.78169	0.09884	0.09883
2.5	0.81891	0.81898	0.05452	0.05451
3.0	0.83933	0.83939	0.02951	0.02950

Table 2 Results by Runge–Kutta method (RKM) and present method with $N = 201$ (Isothermal)

η	$H(\eta)$		$\theta(\eta)$	
	RKM	Present method	RKM	Present method
0.0	1.4E-23	0.00000	1.00000	1.00000
0.5	0.01822	0.01831	0.73413	0.73420
1.0	0.02772	0.02790	0.51234	0.51245
1.5	0.03199	0.03224	0.34660	0.34675
2.0	0.03309	0.03341	0.23024	0.23042
2.5	0.03229	0.03265	0.15137	0.15156
3.0	0.03035	0.03075	0.09893	0.09913

$\mathrm{TOL} = 1\mathrm{E}-8$. The initial guess in Newton's method for isothermal wall temperature condition and isofux boundary condition are taken as:

Isothermal: $g_1(\eta) = \lambda, g_2(\eta) = 1, g_3(\eta) = 0, g_4(\eta) = 0, g_5(\eta) = 0, g_6(\eta) = 1, g_7(\eta) = 0.$

Isoflux: $g_1(\eta) = \lambda, g_2(\eta) = 1, g_3(\eta) = 0, g_4(\eta) = 0, g_5(\eta) = 0, g_6(\eta) = 0, g_7(\eta) = -1.$

Results and discussion

Here, the numerical study of fluid flow and heat transfer in micropolar fluids through porous medium due to a permeable stretching sheet has been performed using nonstandard finite difference approximation. Isothermal wall temperature condition and isoflux boundary condition are considered in this investigation. The influence of the various physical parameters, namely the Reynolds number, Prandtl number, micropolar material parameters, injection/suction parameter, heat index parameter on flow speed, temperature distribution, and spin behavior of microstructures are presented graphically. The good agreement of the numerical results obtained by the current method with the Runge–Kutta method demonstrates the validity of our findings. The fixed values of the various physical parameters considered in this study are taken as: $c_1 = 0.5$, $c_2 = 0.1$, $c_3 = 0.5$, $\lambda = 0$, $P_r = 1$, $R_e = 1$. For isothermal and isoflux boundary conditions $s = 0$ and $s = 1$ have been taken. Tables 1 and 3 show the comparison of flow speed obtained by the current method and Runge–Kutta technique with isothermal and isoflux boundary conditions, respectively. Tables 2 and 4 show a comparison of microrotation and temperature distribution by the present method and Runge–Kutta method with isothermal and isoflux boundary conditions, respectively. The numerical results by both the methods have an excellent agreement in Tables 1–4, which validates our study.

The effect of injection/suction parameter (λ) on flow speed $f'(\eta)$ under isothermal boundary condition has been shown in Fig. 1. The increasing value of λ reduces the boundary layer thickness, i.e., it decreases the flow speed.

Table 3 Results by Runge–Kutta method (RKM) and present method with $N = 201$ (Isoflux)

η	$f(\eta)$		$f'(\eta)$	
	RKM	Present method	RKM	Present method
0.0	0.00000	0.00000	1.00000	1.00000
0.5	0.38025	0.38024	0.56255	0.56251
1.0	0.59401	0.59398	0.31592	0.31587
1.5	0.71390	0.71384	0.17684	0.17679
2.0	0.78085	0.78078	0.09841	0.09839
2.5	0.81796	0.81789	0.05422	0.05422
3.0	0.83826	0.83822	0.02936	0.02940

Table 4 Results by Runge–Kutta method (RKM) and present method with $N = 201$ (Isoflux)

η	$H(\eta)$		$\theta(\eta)$	
	RKM	Present method	RKM	Present method
0.0	−1.1E-30	0.00000	1.25457	1.25460
0.5	0.01652	0.01627	0.88499	0.88502
1.0	0.02439	0.02392	0.69459	0.69461
1.5	0.02721	0.02654	0.60110	0.60112
2.0	0.02712	0.02627	0.55823	0.55822
2.5	0.02539	0.02442	0.54067	0.54065
3.0	0.02282	0.02176	0.53506	0.53503

Figure 2 shows effect of λ on dimensionless microrotation $H(\eta)$. The microrotation decreases with an increasing value of λ. It rises near the boundary and then starts decreasing gradually away from it.

The influence of Prandtl number (P_r) with isothermal boundary condition on temperature profile is depicted in Fig. 3. The thickness of the thermal boundary layer reduces with an increasing value of Prandtl number (P_r).

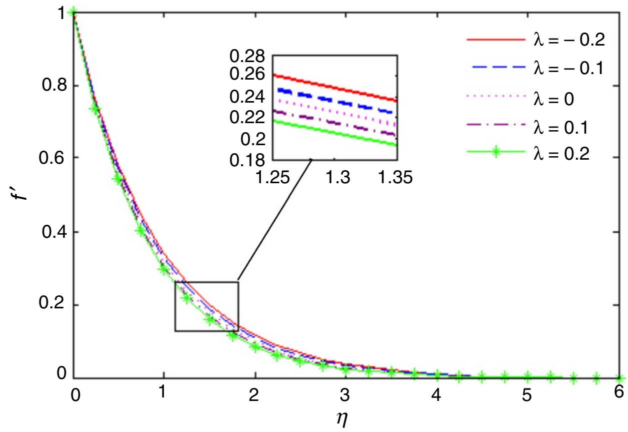

Fig. 1 Effect of λ on f' under isothermal condition

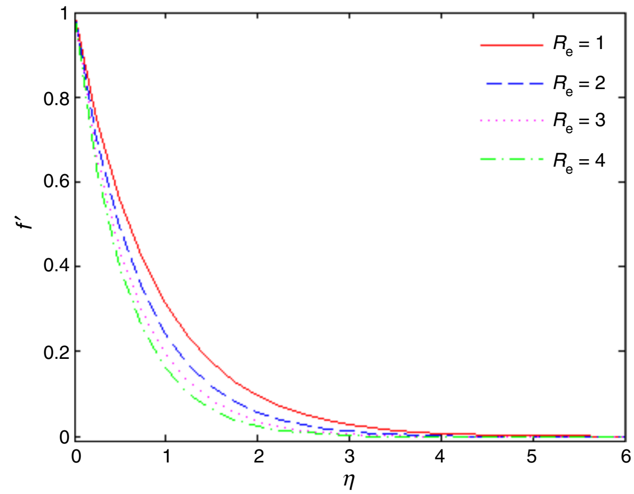

Fig. 4 Effect of (R_e) on f' under isothermal condition

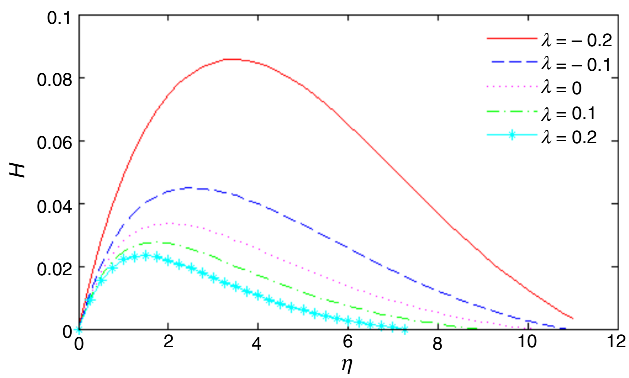

Fig. 2 Effect of λ on H under isothermal condition

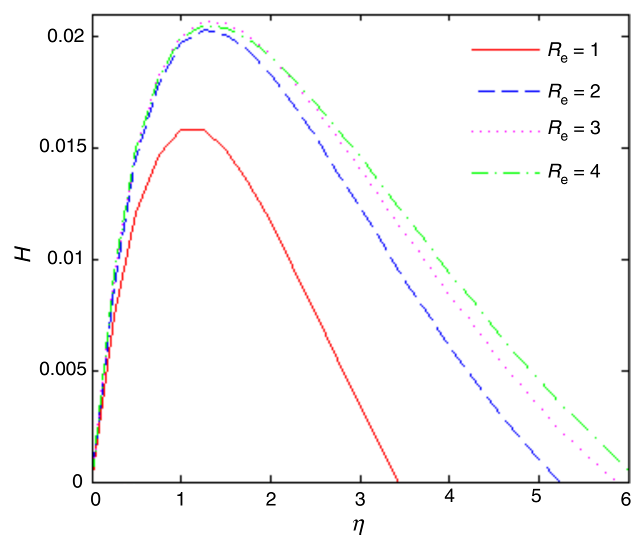

Fig. 5 Effect of (R_e) on H under isothermal condition

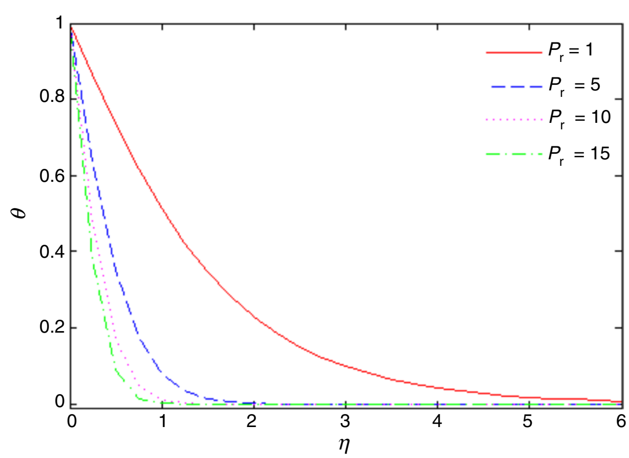

Fig. 3 Effect of (P_r) on θ under isothermal condition

Figure 4 shows that increasing value of Reynolds number (R_e) decreases value of flow speed $(f'(\eta))$, i.e., boundary layer thickness reduces with increasing value of (R_e) under isothermal boundary condition.

Figure 5 shows effect of Reynolds number R_e on dimensionless microrotation $H(\eta)$. The microrotation increases near the boundary with an increasing value of R_e. It decreases gradually away from the boundary.

Figure 6 represents temperature distribution $\theta(\eta)$ for fluid flow with isothermal boundary condition under the influence of heat index parameter s. The thermal boundary layer of fluid flow decreases with an increasing value of s.

Figure 7 shows increment in boundary layer thickness of fluid flow with an increment in micropolar parameter c_1, i.e., under isothermal boundary condition, with an increasing value of c_1 flow speed $f'(\eta)$ increases.

Figure 8 demonstrates the thermal behavior of the fluid under the influence of micropolar parameter c_1. The

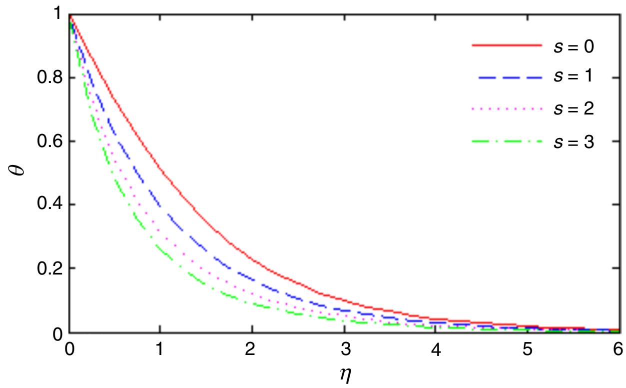

Fig. 6 Effect of s on θ under isothermal condition

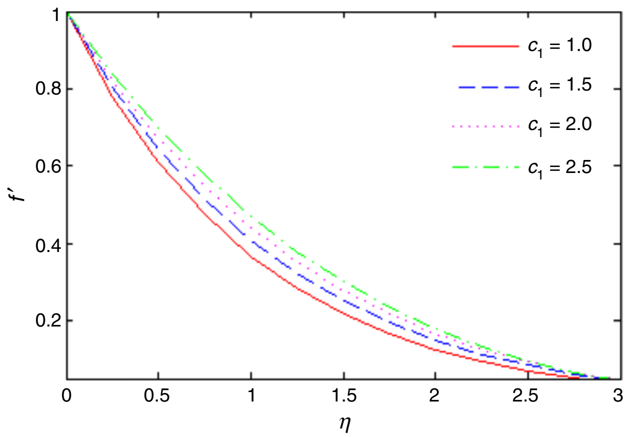

Fig. 7 Effect of c_1 on f' under isothermal condition

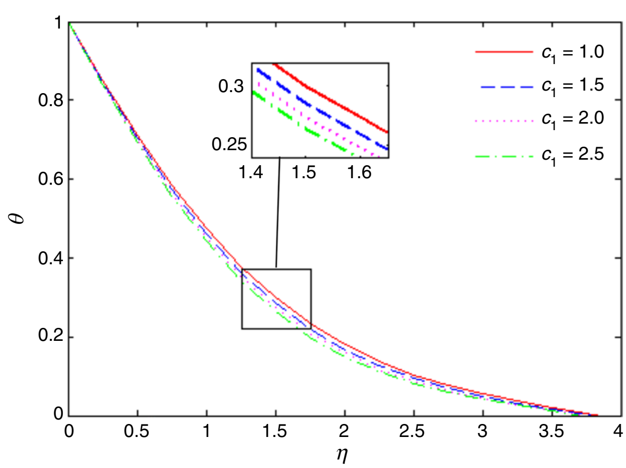

Fig. 8 Effect of c_1 on θ under isothermal condition

thermal boundary layer decreases with the increasing value of micropolar parameter c_1. Figures 7 and 8 show that the effect of c_1 on flow speed and temperature distribution are opposite.

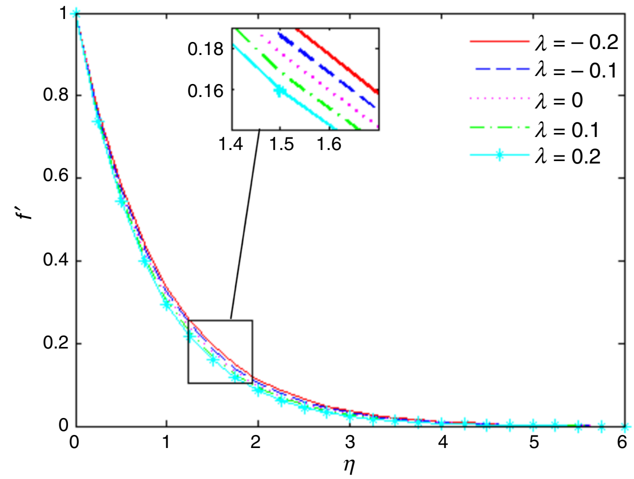

Fig. 9 Effect of λ on f' under isoflux condition

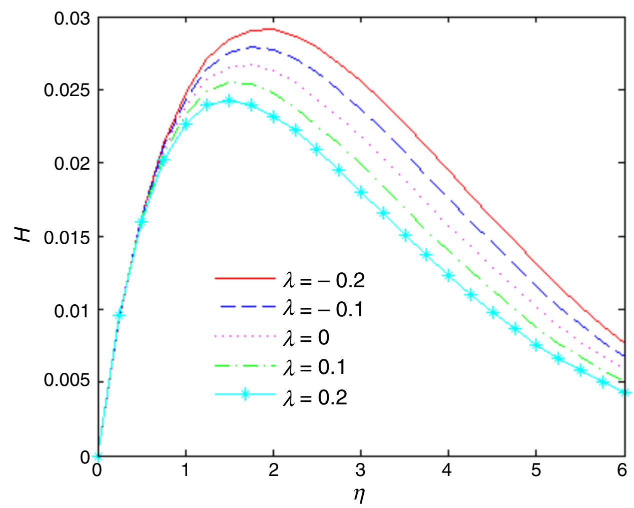

Fig. 10 Effect of λ on H under isoflux condition

The effect of injection/suction parameter λ on flow speed $f'(\eta)$ with isoflux boundary condition is shown in Fig. 9. Figure 9 shows that flow speed reduces with an increasing value of λ. Hence, from Figs. 1 and 9, it is remarkable that for isothermal as well as isoflux boundary conditions, the effect of λ on flow speed is the same.

Figure 10 displays the effect of λ on dimensionless microrotation $H(\eta)$ under isoflux boundary condition. The microrotation decreases with an increasing value of λ. It increases near the boundary then starts decreasing gradually away from the boundary. From Figs. 10 and 2, it is found that the influence of the injection/suction parameter on microrotation is the same for isothermal and isoflux boundary conditions.

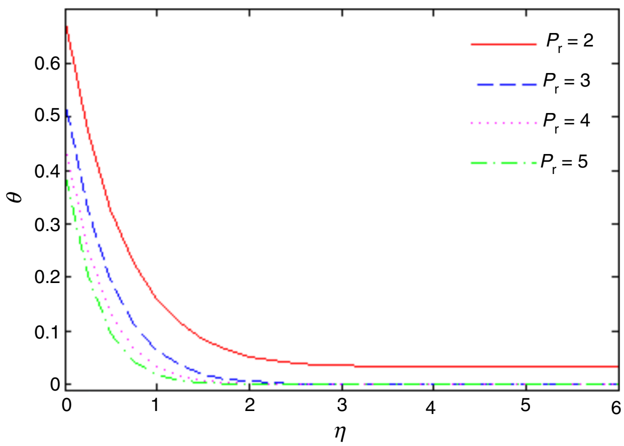

Fig. 11 Effect of P_r on θ under isoflux condition

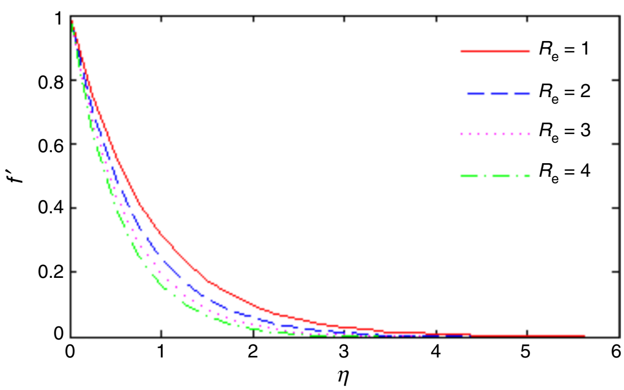

Fig. 12 Effect of R_e on f' under isoflux condition

In Fig. 11, effect of Prandtl number (P_r) on temperature profile under isoflux boundary condition is presented. The thickness of thermal boundary layer reduces with an increasing value of Prandtl number (P_r), which is the same as in the isothermal boundary condition.

The effect of Reynolds number (R_e) on flow speed $f'(\eta)$ under isoflux boundary condition is shown in Fig. 12. The boundary layer thickness reduces with an increasing value of R_e. The effect of Reynolds number on the boundary layer thickness for both types of boundary conditions is the same.

Figure 13 represents influence of the Reynolds number (R_e) on dimensionless microrotation $H(\eta)$ under isoflux boundary condition. The microrotation increases near the boundary with an increasing value of R_e. Figure 13 shows gradual decrease in $H(\eta)$ away from the boundary.

The influence of the heat index s on temperature profile $\theta(\eta)$ under isoflux boundary condition is depicted in Fig. 14. The thermal boundary layer of fluid flow reduces with an increasing value of s.

Figure 15 shows increment in boundary layer thickness of fluid flow with an increment in micropolar parameter c_1, i.e., under isoflux boundary condition, with an increasing value of c_1 flow speed $f'(\eta)$ increases.

Figure 16 demonstrates the thermal behavior of the fluid under the influence of micropolar parameter c_1. The

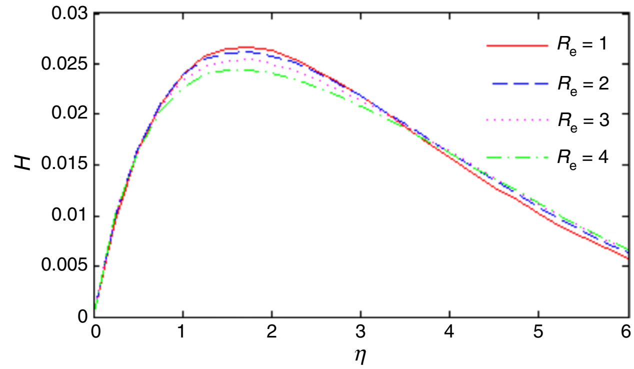

Fig. 13 Effect of R_e on H under isoflux condition

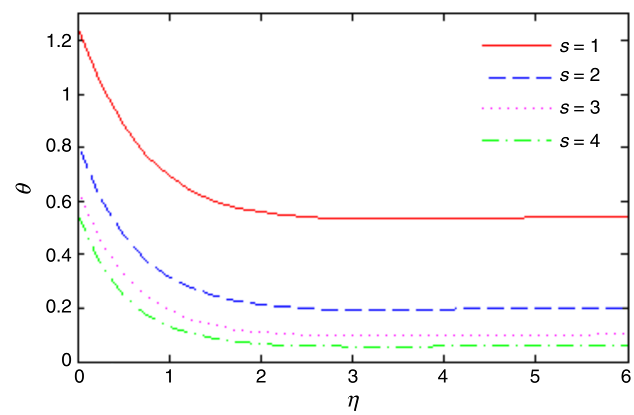

Fig. 14 Effect of s on θ under isoflux condition

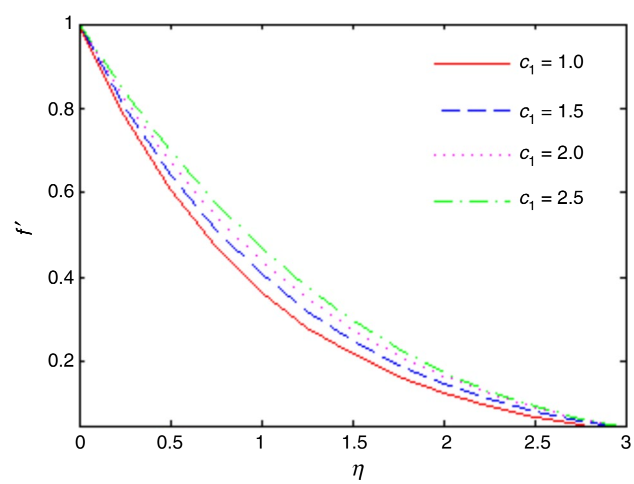

Fig. 15 Effect of c_1 on f' under isoflux condition

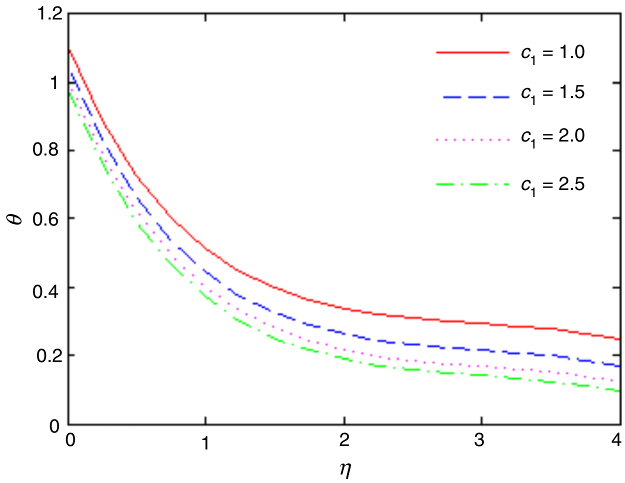

Fig. 16 Effect of c_1 on θ under isoflux condition

thermal boundary layer decreases with the increasing value of micropolar parameter c_1. Figures 15 and 16 show that the effect of c_1 on flow speed and temperature distribution are opposite. Hence, from Figs. 7, 8, 15, and 16, it is clear that the effect of micropolar parameter c_1 on boundary layer thickness and thermal boundary layer thickness remains the same for the isothermal as well as the isoflux boundary conditions.

Conclusions

In this work, fluid flow, heat transfer, and microrotation of micropolar fluids with isothermal and isoflux boundary conditions have been studied using nonstandard finite difference approximation. The validity of our numerical results has been proved by comparing these with those obtained by the Runge–Kutta method. The findings of this study are concluded as follows:

- The increasing value of the injection/suction parameter (negative to positive) reduces the thickness of boundary layer.
- The increasing value of the injection/suction parameter (negative to positive) increases microrotation of the microstructures near the boundary.
- For isothermal as well as isoflux boundary conditions, increasing the Reynolds number reduces the thickness of the fluid flow boundary layer.
- The increasing value of the micropolar parameter reduces the thermal boundary layer thickness for both types of boundary conditions (isothermal and isoflux).
- The increasing value of the micropolar parameter increases the boundary layer thickness of flow under isothermal as well as isoflux boundary conditions.
- The thickness of the thermal boundary layer reduces with the increasing value of Prandtl number and heat index parameter for both types of boundary conditions (isothermal and isoflux).

Acknowledgements The authors of this study would like to express their sincere thanks to all the three anonymous reviewers and the editor for their valuable comments / suggestions to make this work more effective and insightful.

References

1. Hussanan A, Salleh MZ, Khan I, Tahar RM. Heat and mass transfer in a micropolar fluid with newtonian heating: an exact analysis. Neural Comput Appl. 2018;29(6):59–67.
2. Akram N, Sadri R, Kazi S, Ahmed S, Zubir M, Ridha M, Soudagar M, Ahmed W, Arzpeyma M, Tong GB. An experimental investigation on the performance of a flat-plate solar collector using eco-friendly treated graphene nanoplatelets-water nanofluids. J Therm Anal Calorim. 2019;138(1):609–21.
3. Akram N, Sadri R, Kazi S, Zubir MNM, Ridha M, Ahmed W, Soudagar MEM, Arzpeyma M. A comprehensive review on nanofluid operated solar flat plate collectors. J Therm Anal Calorim. 2020;139(2):1309–43.
4. Ahmed W, Chowdhury Z, Kazi S, Johan M, Akram N, Oon C. Effect of zno-water based nanofluids from sonochemical synthesis method on heat transfer in a circular flow passage. Int Commun Heat Mass Transf. 2020;114:104591.
5. Ahmed W, Zaman Chowdhury Z, Kazi SN, Johan M, Bin R, Badruddin IA, Soudagar MEM, Kamangar S, Mujtaba MA, Gul M, et al. Evaluation on enhanced heat transfer using sonochemically synthesized stable zno-eg@ dw nanofluids in horizontal calibrated circular flow passage. Energies. 2021;14(9):2400.
6. Ahmed W, Kazi S, Chowdhury Z, Johan MRB, Mehmood S, Soudagar MEM, Mujtaba M, Gul M, Ahmad MS. Heat transfer growth of sonochemically synthesized novel mixed metal oxide ZnO + Al_2O_3 + TiO_2/DW based ternary hybrid nanofluids in a square flow conduit. Renew Sustain Energy Rev. 2021;145:111025.
7. Sulochana C, Aparna S, Sandeep N. Heat and mass transfer of magnetohydrodynamic casson fluid flow over a wedge with thermal radiation and chemical reaction. Heat Transfer. 2021;50(4):3704–21.
8. Eringen AC. Theory of micropolar fluids. J Math Mech. 1966;1–18.
9. Ahmad F, Almatroud AO, Hussain S, Farooq SE, Ullah R. Numerical solution of nonlinear diff. equations for heat transfer in micropolar fluids over a stretching domain. Mathematics. 2020;8(5):854.
10. Sakiadis BC. Boundary-layer behavior on continuous solid surfaces: I. Boundary-layer equations for two-dimensional and axisymmetric flow. AIChE J. 1961;7(1):26–8.
11. Sakiadis B. Boundary-layer behavior on continuous solid surfaces: II. The boundary layer on a continuous flat surface. AIChE J. 1961;7(2):221–5.
12. Sakiadis B. Boundary-layer behavior on continuous solid surfaces: III. The boundary layer on a continuous cylindrical surface. AIChE J. 1961;7(3):467–72.
13. Crane LJ. Flow past a stretching plate. Zeitschrift für angewandte Mathematik und Physik ZAMP. 1970;21(4):645–7.

14. Bachok N, Ishak A, Nazar R. Flow and heat transfer over an unsteady stretching sheet in a micropolar fluid. Meccanica. 2011;46(5):935–42.
15. Nazar R, Amin N, Filip D, Pop I. Stagnation point flow of a micropolar fluid towards a stretching sheet. Int J Non-Linear Mech. 2004;39(7):1227–35.
16. Mohanty B, Mishra S, Pattanayak H. Numerical investigation on heat and mass transfer effect of micropolar fluid over a stretching sheet through porous media. Alex Eng J. 2015;54(2):223–32.
17. Mandal IC, Mukhopadhyay S. Nonlinear convection in micropolar fluid flow past an exponentially stretching sheet in an exponentially moving stream with thermal radiation. Mech Adv Mater Struct. 2019;26(24):2040–6.
18. Jain S, Gupta P. Entropy generation analysis of mhd viscoelasticity-based micropolar fluid flow past a stretching sheet with thermal slip and porous media. Int J Appl Comput Math. 2019;5(3):1–22.
19. Ramadevi B, Kumar KA, Sugunamma V, Reddy JR, Sandeep N. Magnetohydrodynamic mixed convective flow of micropolar fluid past a stretching surface using modified fouriers heat flux model. J Therm Anal Calorim. 2020;139(2):1379–93.
20. Mahmoud MA. Thermal radiation effects on mhd flow of a micropolar fluid over a stretching surface with variable thermal conductivity. Phys A. 2007;375(2):401–10.
21. Ishak A, Nazar R, Pop I. Mhd boundary-layer flow of a micropolar fluid past a wedge with constant wall heat flux. Commun Nonlinear Sci Numer Simul. 2009;14(1):109–18.
22. Qasim M, Khan I, Shafie S. Heat transfer in a micropolar fluid over a stretching sheet with Newtonian heating. PLoS ONE. 2013;8(4):e59393.
23. Arifuzzaman S, Mehedi MFU, Al-Mamun A, Biswas P, Islam MK, Khan M. Magnetohydrodynamic micropolar fluid flow in presence of nanoparticles through porous plate: a numerical study. Int J Heat Technol. 2018;36(3):936–48.
24. Eldabe NT, Ouaf ME. Chebyshev finite difference method for heat and mass transfer in a hydromagnetic flow of a micropolar fluid past a stretching surface with ohmic heating and viscous dissipation. Appl Math Comput. 2006;177(2):561–71.
25. Fatunmbi E, Adeniyan A. Heat and mass transfer in mhd micropolar fluid flow over a stretching sheet with velocity and thermal slip conditions. Open J Fluid Dyn. 2018;8:195–215.
26. Khader M, Sharma RP. Evaluating the unsteady mhd micropolar fluid flow past stretching/shirking sheet with heat source and thermal radiation: implementing fourth order predictor-corrector fdm. Math Comput Simul. 2021;181:333–50.
27. Akinshilo AT, Illegbusi A. Laminar viscous flow of micropolar fluid through non-darcy porous medium undergoing uniform suction or injection. AUT J Mech Eng. 2019;3(2):157–64.
28. Patel HR, Singh R. Thermophoresis, brownian motion and nonlinear thermal radiation effects on mixed convection mhd micropolar fluid flow due to nonlinear stretched sheet in porous medium with viscous dissipation, joule heating and convective boundary condition. Int Commun Heat Mass Transfer. 2019;107:68–92.
29. Akhter S, Ashraf M, Ali K. Mhd flow and heat transfer analysis of micropolar fluid through a porous medium between two stretchable disks using quasi-linearization method. Iran J Chem Chem Eng (IJCCE). 2017;36(4):155–69.
30. Ahmad S, Ashraf M, Ali K. Numerical simulation of viscous dissipation in a micropolar fluid flow through a porous medium. J Appl Mech Tech Phys. 2019;60(6):996–1004.
31. Ahmad S, Ashraf M, Ali K. Simulation of thermal radiation in a micropolar fluid flow through a porous medium between channel walls. J Therm Anal Calorim. 2021;144(3):941–53.
32. Shehzad S, Abbas Z, Rauf A. Finite difference approach and successive over relaxation (sor) method for mhd micropolar fluid with maxwell-cattaneo law and porous medium. Phys Scr. 2019;94(11):115228.
33. Abro KA, Khan I, Gómez-Aguilar J. Thermal effects of magnetohydrodynamic micropolar fluid embedded in porous medium with fourier sine transform technique. J Braz Soc Mech Sci Eng. 2019;41(4):1–9.
34. Jangili S, Adesanya S, Falade J, Gajjela N. Entropy generation analysis for a radiative micropolar fluid flow through a vertical channel saturated with non-darcian porous medium. Int J Appl Comput Math. 2017;3(4):3759–82.
35. Eldabe NT, Ramadan SF. Impacts of peristaltic flow of micropolar fluid with nanoparticles through a porous medium under the effects of heat absorption and wall properties: Homotopy perturbation method. Heat Transfer. 2020;49(2):889–908.
36. Ferdows M, Shamshuddin M, Zaimi K. Dissipative-radiative micropolar fluid transport in a nondarcy porous medium with cross-diffusion effects. CFD Lett. 2020;12(7):70–89.
37. Naganthran K, Md Basir MF, Thumma T, Ige EO, Nazar R, Tlili I. Scaling group analysis of bioconvective micropolar fluid flow and heat transfer in a porous medium. J Therm Anal Calorim. 2021;143:1943–55.
38. Lund LA, Omar Z, Khan I, Raza J, Sherif E-SM, Seikh AH. Magnetohydrodynamic (mhd) flow of micropolar fluid with effects of viscous dissipation and joule heating over an exponential shrinking sheet: triple solutions and stability analysis. Symmetry. 2020;12(1):142.
39. Kumar KA, Sugunamma V, Sandeep N. Influence of viscous dissipation on mhd flow of micropolar fluid over a slendering stretching surface with modified heat flux model. J Therm Anal Calorim. 2020;139(6):3661–74.
40. Guram G, Smith A. Stagnation flows of micropolar fluids with strong and weak interactions. Comput Math Appl. 1980;6(2):213–33.
41. Jena SK, Mathur M. Similarity solutions for laminar free convection flow of a thermomicropolar fluid past a non-isothermal vertical flat plate. Int J Eng Sci. 1981;19(11):1431–9.
42. Ahmadi G. Self-similar solution of imcompressible micropolar boundary layer flow over a semi-infinite plate. Int J Eng Sci. 1976;14(7):639–46.
43. Peddieson J Jr. An application of the micropolar fluid model to the calculation of a turbulent shear flow. Int J Eng Sci. 1972;10(1):23–32.
44. Kamal MA, Ashraf M, Syed K. Numerical solution of steady viscous flow of a micropolar fluid driven by injection between two porous disks. Appl Math Comput. 2006;179(1):1–10.
45. Fazio R, Jannelli A. Finite difference schemes on quasi-uniform grids for bvps on infinite intervals. J Comput Appl Math. 2014;269:14–23.
46. Fazio R, Jannelli A. A non-standard finite difference scheme for magneto-hydro dynamics boundary layer flows of an incompressible fluid past a flat plate. Math Comput Appl. 2021;26(1):22.